Synergistic heat treatment derived hollow-mesoporous-microporous Fe-N-C-SHT electrocatalyst for oxygen reduction reaction

Tao Jiang[a], Weiling Luan[a,*], Yufeng Ren[a], Chenyao Fan[b], Qi Feng[b], Lyudmila Turyanska[c]

a. Key Laboratory of Pressure Systems and Safety (MOE), School of Mechanical and Power Engineering, East China University of Science and Technology, Shanghai 200237, China.

b. SAIC Motorcycle Company, Prospective Technology Department, Shanghai 201800, China.

c. Faculty of Engineering, University of Nottingham, University Park, NG72RD, UK

Corresponding author: luan@ecust.edu.cn

ABSTRACT: Exploring an economical and efficient oxygen reduction reaction (ORR) is an essential but challenging field of study. Metal–organic frameworks (MOFs) have emerged as promising candidates for the preparation of porous catalysts. Here we propose a synergistic heat treatment (SHT) method to synthesize Fe-N-C-SHT catalyst with hierarchical porous hollow structures via a simple carbonization method by the synergistic heating of ZIF-8-Fe (ZIF-8 doped with Fe) and ZIF-67 in a tube furnace. Fe-N-C-SHT catalyst displays efficient ORR activity (half-wave potential (E_{half}) = 0.88 V versus reversible hydrogen electrode (RHE) with a loading of 0.204 $mg_{Fe\text{-}N\text{-}C\text{-}SHT}cm^{-2}$), which is superior to that of Fe-N-C synthesized using individual heat treatment (IHT) (E_{half} = 0.84 V) and Pt/C catalyst (E_{half} = 0.86 V). We achieve enhanced catalytic properties, enhanced methanol tolerance, and long-term durability of the Fe-N-C-SHT catalyst in alkaline electrolyte. The improved ORR activity is attributed to the synergistic effect of Fe doping and optimized SHT methodology, which led to the formation of a highly porous catalyst with numerous active sites. The developed SHT method presents a novel route to fabricate Fe-N-C catalysts with hollow-mesoporous-microporous structures and high performance in ORR.

Keywords: hollow-mesoporous-microporous; synergistic heat treatment; Fe-N-C; oxygen reduction reaction; catalyst

1. Introduction

Fuel cells (FCs) such as proton exchange membrane fuel cells (PEMFCs) and alkaline fuel cells (AFCs) are powered via electrochemical reactions have attracted increasing attention and are considered advantageous because of their high power density and environment friendliness [1, 2]. However, the slow rate of oxygen reduction reaction (ORR) kinetics requires prolonged catalysis at the cathode, limiting the efficiency of PEMFCs and AFCs [3, 4]. Despite their high cost and low natural abundance, precious metals like Ru-, Pd- and Pt-based materials are employed as catalysts to accelerate ORR [5-7] and are considered efficient catalysts for alkaline environment [8, 9]. Also, the design of two electron process plays an important role in catalyst development, and has attracted significant attention [10, 11]. Currently, metal-nitrogen-doped carbon nanomaterials (M-N-C, where M = Fe, Co, Mn, etc.) are extensively explored as alternative ORR catalysts [12-16]. Among these, Fe-N-C exhibits an activity toward ORR, which is comparable to activity of commercial precious metal catalysts [17-23]. The Fe-Nx coordinated complexes are commonly considered as active centers that change the electron distribution of the adjacent carbon and enhance its catalytic activity [24, 25].

A hierarchical porous structure of the catalyst is essential, with macropores facilitating the transfer of reactants and products, mesopores providing large specific surface areas, and micropores offering high-density active sites [13, 26]. Metal–organic frameworks (MOFs) have been utilized as potential precursors to prepare M-N-C based

ORR catalysts because of their large specific surface areas (>1,000 m^2 g^{-1}), uniform hierarchical porous structures, high nitrogen and carbon contents, high structural stability, and ease of doping [27-31]. Among them, the typical MOFs are zeolite imidazole frameworks (ZIFs), such as ZIF-67 and ZIF-8 that are porous and contain abundant nitrogen contents, used as precursors for ORR catalysts by hydrothermal synthesis and heat treatment in inert atmospheres [18, 32-38]. In particular, pyrolysis of ZIF-8 is considered to produce abundant graphitic carbon with mesopores and large specific surface areas, which are beneficial to ORR catalytic activity [39]. To date, most of the ZIF-based hierarchical porous Fe-N-C catalyst structures combine the mesopores and micropores and do not contain any macropores [34, 36, 38, 40-42]. Catalysts with macropores are mostly produced on solid templates, such as SiO_2 and ZnO, followed by the removal of templates by etching or pyrolysis [43, 44], thus increasing the complexity and toxicity of the procedure and even costs [45]. Thus, the development of new methods for synthesis of ORR catalysts containing all three types of pores, without the need for external templates, is an urgent requirement.

ZIF-8 can easily be doped with transition metals (TM, such as Fe, Co, Mn), by hydrolysis method or double solvents method [18, 46, 47]. During the pyrolysis process, TM catalyzes the ZIF-8 to porous carbon materials and coordinates with N to Fe-Nx active sites or with C to Fe_3C compound, which is also considered beneficial to ORR catalytic activity [21, 25, 28, 48-51]. Here, we report on a synergistic heat treatment (SHT) method to produce Fe-N-C-SHT catalyst with a hollow-mesoporous-

microporous structure by synergistic heating of ZIF-8-Fe (ZIF-8 doped with Fe) and ZIF-67 in a tube furnace. We optimize the SHT method by examining the effect of pyrolysis temperature, different TM (Fe, Co, Mn), and contents of doped Fe used on the structure and porosity of the catalyst. We achieve the formation of hollow-mesoporous-microporous Fe-N-C-SHT catalyst having an ORR activity (half-wave potential E_{half} = 0.88 V) higher than that of hollow structure-free Fe-N-C catalyst (E_{half} = 0.84 V) produced by conventional individual heat treatment (IHT) and by SHT without metal doping N@C catalyst (E_{half} = 0.77 V) in alkaline electrolyte (0.1 M KOH). The activity of Fe-N-C-SHT toward ORR is also enhanced with a positive half-wave potential (20 mV) compared to that of Pt/C 20 wt.%. Additionally, this Fe-N-C-SHT catalyst has enhanced methanol tolerance and long-term durability in 0.1 M KOH solution. From the results of our spectroscopic studies, we attribute the enhanced ORR activity of Fe-N-C-SHT to the synergistic effect of Fe doping and SHT-derived hollow-mesoporous-microporous structure with greater number of active sites.

2. Experimental

2.1. Synthesis of ZIF-67 and ZIF-8

All the chemicals used in this study were purchased from Aladdin; they were used without further purification. To synthesize ZIF-8, 594.98 mg (2 mmol) of zinc nitrate hexahydrate ($Zn(NO_3)_2$•$6H_2O$) were dissolved in 16 mL of anhydrous methanol and stirred for 5 minutes. Then 656.8 mg (8 mmol) of dimethylimidazole dissolved in 16 mL of methanol were added dropwise into the

former solution. After stirring for 6 hours at room temperature, the solution was centrifuged at 5,000 rpm and washed with methanol three times. The solid product was dried in vacuum oven for 12 hours at 60 °C. The synthesis of ZIF-67 was realized by employing the same procedure with 582.06 mg (2 mmol) of cobalt nitrate hexahydrate. The white product was ZIF-8 and purple product was ZIF-67.

2.2. Synthesis of ZIF-8-Fe (ZIF-8-Co and ZIF-8-Mn)

To prepare ZIF-8-Fe, 100 mg of ZIF-8 were dissolved in 16 mL of methanol and ultrasonicated (ShuMei, KQ3200DV, 90 Hz) for 20 minutes. Then different volumes of 150 μL (50, 100, 200, 250 μL) of 50 mg mL^{-1} aqueous solution of ferric chloride hexahydrate ($FeCl_3$•$6H_2O$) were injected into the former solution to investigate the optimal doping amount of iron. After being ultrasonicated for 2 hours at 25 °C, the solution was stirred for 1 hour at 500 rpm, centrifuged at 5,000 rpm, and washed two times with methanol. Finally, the white-yellow ZIF-8-Fe powder was collected after vacuum drying for 12 hours at 60 °C. Samples with other metals, ZIF-8-Co and ZIF-8-Mn, were prepared via the same method except by doping 150 μL of 50 mg mL^{-1} aqueous solution of cobalt(II) acetate tetrahydrate ($C_4H_6CoO_4$·$4(H_2O)$) and 150 μL of 50 mg mL^{-1} aqueous solution of manganese(II) chloride ($MnCl_2$).

2.3. Synergistic heat treatment of ZIF–8–Fe (ZIF–8–Co and ZIF–8–Mn) with ZIF–67

The powders of ZIF-67 (100 mg) and ZIF-8 (-M) (100 mg) were pyrolyzed in a quartz tube in a furnace at different temperatures, T = 900 °C (700, 800, 1000 °C). A ceramic boat with powder of ZIF-67 was placed next to ZIF-8-Fe, and they were heated under Ar atmosphere at a heating rate of 5 °C min^{-1}, pyrolyzed for 2 hours, and cooled in the furnace to T = 60 °C. For all SHT processes, ZIF-67 was placed at the outlet of argon. The black powders of Fe-N-C-SHT, Co-N-C-SHT, and Mn-N-C-SHT were collected.

2.4. Preparation of N@C and individual heat treatment of ZIF-8-M (M=Fe, Co, Mn)

To examine the effect of metal doping, N@C catalyst was prepared by SHT of ZIF-8 and ZIF-67 at 900 °C for 2 hours. To investigate the effect of ZIF-67 on ZIF-8-M (M = Fe, Co, Mn), we prepared Fe-N-C, Co-N-C-I (to distinguish it from SHT of ZIF-67 derived Co-N-C) and Mn-N-C catalysts by the IHT of ZIF-8-Fe, ZIF-8-Co, and ZIF-8-Mn at 900 **°C** for 2 hours.

2.5. Materials characterization

The morphology of all samples was studied using field emission scanning electron microscopy (FESEM, Hitachi Limited S-4800) and high-resolution transmission electron microscopy (HRTEM, JEOL JEM-2100F). For the elemental mapping, the scanning transmission electron microscope (STEM) was operated at 200 kV with a high-angle annular-dark-field (HAADF) detector (Hitachi S-5500). The morphology

was also examined with another high-resolution transmission electron microscopy (HRTEM, FEI Tecnai G2 T20). X-ray powder diffraction (XRD) patterns were recorded on Rigaku 2550VB. For chemical and compositional analysis, X-ray photoelectron spectroscopy (XPS, Thermo ESCALAB250) and inductively coupled plasma atomic emission spectroscopy (ICP-AES, Baird PS-6) were used. The degree of graphitization of the electrocatalysts was investigated by Raman spectroscopy (LabRAM ARAMIS). Brunauer–Emmet–Teller (BET) specific surface area and Barrett–Joyner–Halenda (BJH) pore size distribution of the products were measured with nitrogen adsorption–desorption (Mike ASAP 2020 HD88) isotherm curve at 77 K.

2.6. Electrochemical measurements

All the electrochemical measurements were obtained using a CHI 760E electrochemical workstation (CH Instruments, Chenhua, China) in a conventional three-electrode cell. A silver/silver chloride electrode (Ag/AgCl) and graphite rod electrode were used as the reference electrode as counter electrode, respectively. For the preparation of catalyst inks, 5 mg of the prepared catalyst was dissolved in ultrasound bath for 2 hours in a mixture solution of 60 μL Nafion (5 wt.%) solution, 470 μL ultrapure water, and 470 μL ethanol. Five milligrams of 20 wt.% Pt/C were ultrasonically dispersed into 960 μL isopropanol and 40 μL Nafion. Then 8 μL of catalyst ink were deposited on the glass carbon (GC) rotating disk-ring electrode (RRDE) (4 mm in diameter for disk and 1 mm for ring) and dried in air (at room temperature) for 30 minutes.

This resulted in a catalyst loading of 0.204 mg cm^{-2}. In alkaline media, N_2 or O_2-saturated electrolyte solution, the electrode was activated with 50 cycles of cyclic voltammetry (CV) at a scanning rate of 0.1 V s^{-1} between −1.0 V and 0.2 V at room temperature. The CV curves were measured at a scanning rate of 50 mV s^{-1}. Linear sweep voltammetry (LSV) curves were tested with the RRDE in O_2-saturated 0.1 mol L^{-1} KOH, and the working electrode was rotated at 1600 rpm with a scan rate of 10 mV s^{-1}. Koutecky–Levich (K–L) plots were analyzed at various electrode potentials, and their slopes and linear fit lines were used to calculate the number (*n*) of electrons transferred following the K–L equations:

$$\frac{1}{j} = \frac{1}{j_L} + \frac{1}{j_K} = \frac{1}{Bw^{1/2}} + \frac{1}{j_K} \quad (1)$$

$$B = 0.2nFC_0(D_0)^{2/3}v^{-1/6} \quad (2)$$

$$j_K = nFkC_0 \quad (3)$$

where j refers to the current density, j_L and j_K are the diffusion-limiting and kinetic current density, respectively, w is the rotation rate of RRDE from 400 to 2025 rpm, n denotes the number of electrons transferred per O_2, F denotes the Faraday constant, C_0 denotes the bulk concentration of O_2, D_0 denotes the diffusion coefficient of O_2, v denotes the kinematic viscosity of the electrolyte, and k denotes the electron-transfer rate constant. The constant 0.2 is adopted when the rotating rate is rpm. There is another method for calculating the number of electrons transferred and yield of H_2O_2 with RRDE, given by the following equations:

$$n = \frac{4I_{disk}}{\frac{I_{ring}}{N} + I_{disk}} \quad (4)$$

$$\%H_2O_2 = \frac{200\frac{I_{ring}}{N}}{\frac{I_{ring}}{N} + I_{disk}} \quad (5)$$

where I_{disk} is the disk electrode current, I_{ring} is the ring electrode current, and N is the collection efficiency (0.39) at the ring electrode. The disk electrode was scanned at a rate of 10 mV s^{-1}, while the ring electrode was biased at 1.48 V (vs. RHE).

3. Results and Discussion

A new method of SHT of ZIF-8-M (where M = Fe, Co, Mn) and ZIF-67 was used to prepare a hollow-mesoporous-microporous structure catalyst and our results were compared with the conventional IHT method (Fig. S1a–b). The ZIF-8 and ZIF-67 MOFs have rhombic dodecahedral structures sized 400 ± 50 nm (Fig. 2a and Fig. S1c). In IHT, ZIF-8-M is pyrolyzed individually in a quartz tube. In the SHT method, ZIF-8 (or ZIF-8-M) is placed next to ZIF-67 in a separate boat and both are pyrolyzed together under Ar atmosphere. The morphological properties of the samples are characterized using transmission electron microscopy (TEM) and scanning electron microscopy (SEM). To examine the effect of metal on the formation of pores, we dope ZIF-8 with Fe (ZIF-8-Fe). The electron imaging of ZIF-8-Fe reveals the presence of ~60 nm pores at the surface (Fig. 2b). The XRD patterns of ZIF-8 and ZIF-8-Fe (Fig. 2c) do not show any significant differences; furthermore, ZIF-8-Fe has slightly lower pore volume than ZIF-8 (0.585 and 0.627 cm^3 g^{-1} for ZIF-8-Fe and ZIF-8,

respectively; see Supplementary Information Fig. S2), suggesting that the $FeCl_3 \cdot 6H_2O$ molecules are adsorbed inside the micropores of ZIF-8.

The SEM and TEM images of SHT-produced N@C catalyst with no metal doping revealed no pores or hollow morphology on the N@C surface (Fig. 2d). For Fe-doped ZIF-8, the IHT-derived Fe-N-C structures also display no hollow cavities (Fig. 2e). However, for the Fe-N-C-SHT sample prepared by SHT of ZIF-8-Fe and ZIF-67, we observed the formation of hollow structures with a pore size of ~200 nm, hierarchical porous structures and presence of carbon nanotubes (CNTs) (Fig. 2f). For evaluating the effect of different metals on the formation of hollow-mesoporous-microporous structures, we also used Co- and Mn-containing MOFs to produce catalysts by SHT. We found no noticeable difference in the morphology or ORR activity of Co-N-C-SHT and Mn-N-C-SHT compared to those prepared by IHT (Fig. S3). Since our control experiments show that all samples prepared using individual heat treatment and those prepared using SHT with other TM (ZIF-8-Mn or ZIF-8-Co) do not reveal formation of hollow structures, we suggest that the hollow structure is caused by the combined effect of Fe and ZIF-67 (or Co). During the synergistic heating process, Co vapor from ZIF-67 diffuses to the ZIF-8-Fe and catalyzes the ZIF to form porous structures [52]. Thus, the origin of hollow-mesoporous-microporous structures observed in Fe-N-C-SHT is attributable to the combined catalytic

effect of Fe and Co from ZIF-67 and the SHT method used. Hence, we further optimized the conditions used in the SHT method for ZIF-8-Fe.

We performed SHT at different pyrolysis temperatures, Argon (Ar) flow rates, and different amount of Fe doping (see Supplementary Information, Fig. S4–S6). Ar flow rates of 20, 40, 60, 80, 100, and 120 mL min^{-1} and pyrolysis temperatures of 700 °C, 800 °C, 900 °C, and 1000 °C were examined. No hollow structures were formed at flow rates less than 60 mL min^{-1} and over 120 mL min^{-1}. Only at a flow rate of 80 mL min^{-1}, formation of hollow structures was observed. The optimal pyrolysis temperature for pore formation was found to be 900 °C. Besides, the porosity is also affected by the Fe content used in SHT by using 50, 100, 150, 200, and 250 μL of 50 mg mL^{-1} aqueous solution of $FeCl_3$•$6H_2O$ in SHT. The hollow-mesoporous-microporous structures increased with increasing Fe content up to 150 μL. At higher quantities of Fe, the porosity decreased; furthermore, collapse of large pores and some metal agglomeration was observed. Hence, the optimal conditions for SHT are T = 900 °C, Ar flow rate of 80 mL min^{-1}, and Fe content of 150 μL. The final Fe loading is assessed by ICP MS and in Fe-N-C-SHT it is 1.02 wt.%.

The distribution of metal in a catalyst is important for its performance. Hence, we assess the morphology of these structures by high-resolution TEM (HRTEM), element maps, and element line sweep analysis. The HRTEM images of Fe-N-C-SHT (Fig. 3a–b) related carbon-based structures with graphite-like crystal

lattice with a lattice size of 0.375 nm correspond to the (002) plane. No metal crystallization was observed in the sample containing all metals neither by HR TEM nor by XRD (Fig. 3b–c and Supplementary Information Figure S7). For accurate analysis of Fe content, ICP-AES was used and 1.02 wt.% and 1.47 wt.% of Fe were detected in Fe-N-C-SHT and Fe-N-C, respectively (see Supplementary Information, Table S1). The high-angle annular-dark-field scanning TEM (HAADF-STEM) and elemental maps of Fe-N-C-SHT showed uniform distribution of Fe and N (Fig. 3d), implying that Fe and N were effectively doped into the carbon framework. Elemental profiles (Fig. 3e) confirm the uniform distribution of C, N, and Fe. We envisage that during SHT, Fe may coordinate with N to create Fe-Nx, which would be beneficial for the catalytic activity as these complexes can act as ORR active sites.

Specific surface area and pore size distribution were assessed via the measurements of nitrogen adsorption–desorption isotherms. The type-IV isotherms with sharp uptakes observed at relative pressures below 0.05 and hysteresis loops ranging from 0.4 to 1.0 were clearly observed for Fe-N-C-SHT and Fe-N-C (Fig. 4a and Supplementary Information Fig. S8), suggesting the coexistence of micropores and mesopores. For N@C and Co-N-C, type-IV curves with hysteresis loops of ~0.4–1.0 were observed; however, there was no uptake at low relative pressures, signifying the presence of only mesopores on their surfaces. The BET method was used for calculating the specific surface

areas of the samples, BJH method was employed to investigate the mesopore size distribution, and density functional theory method was utilized to measure the pore size distributions of the micropores and mesopores (see Supplementary Information Table S2). The Fe-N-C-SHT and Fe-N-C have large BET specific surface areas of 1,198 and 1,124 $m^2 g^{-1}$, respectively. Only small increase in the surface area of Fe-N-C-SHT compared to Fe-N-C is likely due to higher Fe-content (1.47 wt.%) in Fe-N-C (Fe-N-C-SHT has 1.02 wt.% Fe), facilitating formation of larger amount of micro- or mesopores. Our results also confirm the coexistence of ~0.5 nm micropores and ~4.6 nm mesopores in both the samples. Interestingly, N@C has a larger specific surface area of 1,250 $m^2 g^{-1}$ likely because of the uniform three-dimensional distribution of the mesopores with a size of ~3.4 nm. All other samples have small specific surface areas (e.g., 207 $m^2 g^{-1}$ for Co-N-C).

The Raman spectra of Fe-N-C-SHT, Fe-N-C, N@C, and Co-N-C revealed two characteristic peaks of D (1340 cm^{-1}) and G (1590 cm^{-1}) bands of carbon with intensity ratios I_D/I_G of 1.02, 1.01, 1.01, and 0.97, respectively (Fig. 4b and Supplementary Information Fig. S8c). The higher I_D/I_G of ratio observed in Fe-N-C-SHT indicates more disordered carbon, which can improve the catalytic activity in the ORR [53]. A peak at 2700 cm^{-1}, characteristic of two-dimension (2D) carbonization, was observed in the spectra of Fe-N-C-SHT and Co-N-C. We envisage that these peaks confirm the

presence of CNTs, which are likely formed because of the strong catalytic effect of Co from ZIF-67.

The chemical compositions of the catalysts were investigated using XPS (Fig. 4c). The XPS spectrum of Fe-N-C-SHT revealed C–C (284.5 eV), C–N (285.6 eV), C–O (286.6 eV), and O=C–O (289.2 eV) signals. Moreover, pyridinic-N (N_1, 398.4 eV), metal-Nx (N_2, 399.3 eV), pyrrolic-N (N_3, 400.5 eV), quaternary-N (N_4, 401.3 eV), and oxidized-N (N_5, 405.6 eV). The presence of Fe is also validated using XPS, indicating the presence of Fe(II) $2p_{1/2}$ (723.4 eV), Fe(III) $2p_{1/2}$ (726.7 eV), Fe(II) $2p_{3/2}$ (710.2 eV), and Fe(III) $2p_{3/2}$ (713.8 eV) (Fig. 4d–f) [54, 55]. The high-resolution XPS spectra for other samples revealed the same existence of C, N, and Fe for the case of Fe-N-C, and there were no M-N_X coordinated complexes in N@C (see Fig. S9). We note, that presence of oxygen in our samples: 9.35 at% in Fe-N-C-SHT, 12.12 at% in Fe-N-C and 10.36 at% in N@C. We envisage that some oxygen is adsorbed when the samples are transferred from the growth tube and are stored in ambient conditions. We do not expect significant effect of low quantities of oxygen on catalytic activity and focus on the effect of N states like pyridinic or graphitic N, which are significant for ORR. It is well publicized in the literature that pyridinic-N, metal-N, and pyrrolic-N play important roles in the ORR [56-58]. The contents of these types of N for samples are listed in Table S3.

The CV curves revealed a peak potential of 0.85 V for Fe-N-C-SHT, 0.85 V for Pt/C, 0.83 V for Fe-N-C, 0.75 V for N@C, and 0.82 V for Co-N-C (Fig. 5a).

The LSV curves measured using RRDE (Fig. 5b) showed a high value of onset potential (E_{onset}) of 0.96 V for Fe-N-C-SHT and considerably lower values for Pt/C (0.95 V), Fe-N-C (0.93 V), N@C (0.84 V), and Co-N-C (0.88 V). The half-wave potential (E_{half}) also had a greater value for Fe-N-C-SHT (0.88 V) in comparison with other samples (0.86 V for Pt/C, 0.84 V for Fe-N-C, 0.77 V for N@C, and 0.83 V for Co-N-C). Furthermore, Fe-N-C-SHT had a significantly higher limited current density (5.8 mA cm^{-2}) compared to Pt/C (5.2 mA cm^{-2}) and Fe-N-C (4.8 mA cm^{-2}).

From these results, we deduce that Fe-N-C-SHT possesses promising properties for use as a catalyst in ORR. To further investigate the electron-transfer process, the LSV curves were measured at various rotational speeds and the Koutecky–Levich (K–L) plots were used to analyses the kinetics of the reaction. The current density increased with an increase in the rotational speed and the enhanced kinetics is observed with potentials ranging from 0.85 to 0.95 V, indicating first-order reaction kinetics for Fe-N-C-SHT catalyst (Fig. 5c-d). The electron transfer number (n) determined from the RRDE suggests a four-electron transfer pathway and low yield of H_2O_2 (less than 3.5%) for Fe-N-C-SHT (Fig. 5e). The n value at the kinetics limiting region is in the range 3.83 - 3.98. Moreover, the Tafel slope for Fe-N-C-SHT (80 mV dec^{-1}) is much lower than that of Pt/C (103 mV dec^{-1}) and other reference samples (117 mV dec^{-1} for

Fe-N-C, 89 mV dec^{-1} for Co-N-C and 106 mV dec^{-1} for N@C), further confirming its superior ORR catalytic performance (Fig. 5f).

The long-term stability of the Fe-N-C-SHT catalyst was studied by employing an accelerated durability test protocol using a rotating disk electrode (RDE) and comparing it with the Pt/C catalyst. After 20,000 s, we observed ~10% greater stability for Fe-N-C-SHT compared to Pt/C, with relative currents of 95% and 85%, respectively (Fig. 6a). Methanol resistance is also an important requirement for catalyst applications in the proton exchange membrane fuel cells (PEMFCs), particularly for direct methanol fuel cells. Direct injection of 5 mL of 3 M methanol into the electrolyte (50 mL) indicates no modification in the current, with a relative current >97% after 1,000 s. The Pt/C catalyst is very sensitive to methanol and demonstrates a sharp decrease in the current immediately after adding methanol (Fig. 6b). These results further confirm significant advantages of Fe-N-C-SHT as an ORR catalyst. We also note that our SHT-derived Fe-N-C-SHT catalyst has comparable or superior ORR catalytic activity than that of other Fe-ZIF-based catalysts prepared using IHT (see Supplementary Information, Table S4). We attribute the high catalytic performance and enhanced stability of our Fe-N-C-SHT catalyst to the synergistic effect of doping with Fe salts in SHT and the morphology of produced structures, i.e., the hollow-mesoporous-microporous structure. In more challenging acidic electrolyte environment, the Fe-N-C-SHT catalyst shows good performance: E_{half} value of 0.77 V is observed in in 0.1 M $HClO_4$ solution, which is only 80 mV lower than Pt/C and superior than other reference samples (Fig. 6c).

4. Conclusions

In summary, a Fe-N-C-SHT catalyst with a hollow-mesoporous-microporous structure has been successfully prepared using the SHT method, which has been used for the first time to facilitate the formation of a hollow-mesoporous-microporous structure. The Fe-N-C-SHT catalyst exhibits an excellent catalytic activity with respect to the ORR in alkaline electrolytes. Furthermore, the long-term durability and methanol tolerance of the Fe-N-C-SHT catalyst are outstanding. The high ORR activity can be ascribed to the synergistic effect of the doping of Fe and SHT-derived hollow-mesoporous-microporous structure. Therefore, the SHT method is expected to offer a novel strategy for preparing a high-performance M-N-C ORR catalyst with a hollow-mesoporous-microporous structure.

Conflicts of interest

There are no conflicts to declare.

Acknowledgements

This work was financially supported by SAIC Group Co., Ltd., Passenger Vehicle Company, Department of Prospective Technology (Contract No. 4900070369).

Notes and references

[1] B.C.H. Steele, A. Heinzel, Materials for fuel-cell technologies, Nature 414 (2001) 345-352.

[2] M. Li, Z. Zhao, T. Cheng, A. Fortunelli, C.Y. Chen, R. Yu, Q.H. Zhang, L. Gu, B.V. Merinov, Z.Y. Lin, E.B. Zhu, T. Yu, Q.Y. Jia, J.H. Guo, L. Zhang, W.A. Goddard III, Y. Huang, D.X. H., Ultrafine jagged platinum nanowires enable ultrahigh mass activity for the oxygen reduction reaction, Science 354 (2016) 1414-1419.

[3] G. Wu, K.L. More, C.M. Johnston, P. Zelenay, High-performance electrocatalysts for oxygen reduction derived from polyaniline, iron, and cobalt, Science 332 (2011) 443-447.

[4] X. Huang, Z. Zhao, L. Cao, Y. Chen, E. Zhu, Z. Lin, M. Li, A. Yan, A. Zettl, Y.M. Wang, X. Duan, T. Mueller, Y. Huang, High-performance transition metal-doped Pt3Ni octahedra for oxygen reduction reaction, Science 348 (2015) 1230-1234.

[5] F.D. Kong, L.J. Yang, J. Liu, A.X. Ling, M.J. Shi, M. Lv, Z.Q. Xu, Y.L. Niu, H.Y. Wang, Fabrication of Pt/IrO2Nb2O5–rGO electrocatalyst by support improvement for oxygen reduction reaction, Catal. Lett. 149 (2019) 3041-3047.

[6] R. Lin, L. Che, D. Shen, X. Cai, High durability of Pt-Ni-Ir/C ternary catalyst of PEMFC by stepwise reduction synthesis, Electrochim. Acta 330 (2020) 135251.

[7] Q. Hu, W. Zhan, Y. Guo, L. Luo, R. Zhang, D. Chen, X. Zhou, Heat treatment bimetallic PdAu nanocatalyst for oxygen reduction reaction, J. Energy Chem. 40 (2020) 217-223.

[8] X. Wang, Z. Li, Y. Qu, T. Yuan, W. Wang, Y. Wu, Y. Li, Review of metal catalysts for oxygen reduction reaction: From nanoscale engineering to atomic design, Chem 5 (2019) 1486-1511.

[9] X. Ren, Q. Lv, L. Liu, B. Liu, Y. Wang, A. Liu, G. Wu, Current progress of Pt and Pt-based electrocatalysts used for fuel cells, Sustain. Energy Fuels 4 (2019) 15-30.

[10] J.H. Kim, Y.T. Kim, S.H. Joo, Electrocatalyst design for promoting two-electron oxygen reduction reaction: Isolation of active site atoms, Curr. Opin. Electrochem. 21 (2020) 109-116.

[11] G.L. Chai, Z. Hou, T. Ikeda, K. Terakura, Two-electron oxygen reduction on carbon materials catalysts: Mechanisms and active sites, J. Phys. Chem. C 121 (2017) 14524-14533.

[12] F. Tang, H. Lei, S. Wang, H. Wang, Z. Jin, A novel Fe-N-C catalyst for efficient oxygen reduction reaction based on polydopamine nanotubes, Nanoscale 9 (2017) 17364-17370.

[13] H. Mei, M. Yang, Y. Shen, F. He, Z. Zhou, X. Chen, Y. Yang, S. Liu, Y. Zhang, Non-covalent pre-organization of molecular precursors: A facile

approach for engineering structures and activities of pyrolyzed Co-N-C electrocatalysts, Carbon 144 (2019) 312-320.

[14] K. Yu, P.H. Shi, J.C. Fan, Y.L. Min, Q.J. Xu, Porous Fe, Co, and N-co-doped carbon nanofibers as high-efficiency oxygen reduction catalysts, J. Nanopart. Res. 21 (2019) 230.

[15] G.A. Ferrero, N. Diez, M. Sevilla, A.B. Fuertes, Iron/Nitrogen co-doped mesoporous carbon synthesized by an endo-templating approach as an efficient electrocatalyst for the oxygen reduction reaction, Micropor. Mesopor. Mat., 278 (2019) 280-288.

[16] X. Chen, F. He, Y. Shen, Y. Yang, H. Mei, S. Liu, T. Mori, Y. Zhang, Effect of carbon supports on enhancing mass kinetic current density of Fe-N/C electrocatalysts, Chem. Eur. J. 23 (2017) 14597-14603.

[17] X. Xu, Z. Xia, X. Zhang, R. Sun, X. Sun, H. Li, C. Wu, J. Wang, S. Wang, G. Sun, Atomically dispersed Fe-N-C derived from dual metal-organic frameworks as efficient oxygen reduction electrocatalysts in direct methanol fuel cells, Appl. Catal. B Environ. 259 (2019) 118042.

[18] F. Li, X.B. Ding, Q.C. Cao, Y.H. Qin, C. Wang, A ZIF-derived hierarchically porous Fe-Zn-N-C catalyst synthesized: via a two-stage pyrolysis for the highly efficient oxygen reduction reaction in both acidic and alkaline media, Chem. Commun.55 (2019) 13979-13982.

[19] J.W. Huang, Q.Q. Cheng, Y.C. Huang, H.C. Yao, H.B. Zhu, H. Yang, Highly efficient Fe-N-C electrocatalyst for oxygen reduction derived from core-shell-structured Fe(OH)3@zeolitic imidazolate framework, ACS Appl. Energy Mater. 2 (2019) 3194-3203.

[20] L. Gao, M. Xiao, Z. Jin, C. Liu, J. Zhu, J. Ge, W. Xing, Correlating Fe source with Fe-N-C active site construction: Guidance for rational design of high-performance ORR catalyst, J. Energy Chem. 27 (2018) 1668-1673.

[21] D. Guo, S. Han, R. Ma, Y. Zhou, Q. Liu, J. Wang, Y. Zhu, In situ formation of iron-cobalt sulfides embedded in N,S-doped mesoporous carbon as efficient electrocatalysts for oxygen reduction reaction, Micropor. Mesopor. Mat., 270 (2018) 1-9.

[22] R. Wu, J. Wang, K. Chen, S. Chen, J. Li, Q. Wang, Y. Nie, Y. Song, H. Chen, Z. Wei, Space-confined pyrolysis for the fabrication of Fe/N/C nanoparticles as a high performance oxygen reduction reaction electrocatalyst, Electrochim. Acta 244 (2017) 47-53.

[23] S.H. Liu, J.R. Wu, Porous carbon supported Fe-N-C for applications as cathodic electrocatalysts in fuel cells, Micropor. Mesopor. Mat., 170 (2013) 150-154.

[24] L.T. Ma, C.Y. Zhi, Fe, N Doped 2D Porous Carbon Bifunctional Catalyst for Zinc-air Battery, J. Inorg. Mater. 34 (2019) 103-108.

[25] T.N. Tran, C.H. Shin, B.J. Lee, J.S. Samdani, J.D. Park, T.H. Kang, J.S. Yu, Fe-N-functionalized carbon electrocatalyst derived from a zeolitic imidazolate framework for oxygen reduction: Fe and NH3 treatment effects, Catal. Sci. Technol. 8 (2018) 5368-5381.

[26] Q. Li, J. Zhao, M. Wu, C. Li, L. Han, R. Liu, Hierarchical porous N-doped carbon nanofibers supported Fe3C/Fe nanoparticles as efficient oxygen electrocatalysts for Zn−Air batteries, Chem. Select 4 (2019) 722-728.

[27] Y. Wang, J. Wang, D. Wei, M. Li, A "mOF-Protective-Pyrolysis" Strategy for the Preparation of Fe-N-C Catalysts and the Role of Fe, N, and C in the Oxygen Reduction Reaction in Acidic Medium, ACS Appl. Mater. Inter. 11 (2019) 35755-35763.

[28] H. Jin, H. Zhou, D. He, Z. Wang, Q. Wu, Q. Liang, S. Liu, S. Mu, MOF-derived 3D Fe-N-S co-doped carbon matrix/nanotube nanocomposites with advanced oxygen reduction activity and stability in both acidic and alkaline media, Appl. Catal. B Environ. 250 (2019) 143-149.

[29] X. Chen, N. Wang, K. Shen, Y. Xie, Y. Tan, Y. Li, MOF-derived isolated Fe atoms implanted in N-doped 3D hierarchical carbon as an efficient ORR electrocatalyst in both alkaline and acidic media, ACS Appl. Mater. Inter. 11 (2019) 25976-25985.

[30] X. Wang, H. Zhang, H. Lin, S. Gupta, C. Wang, Z. Tao, H. Fu, T. Wang, J. Zheng, G. Wu, X. Li, Directly converting Fe-doped metal-organic

frameworks into highly active and stable Fe-N-C catalysts for oxygen reduction in acid, Nano Energy 25 (2016) 110-119.

[31] M. Yin, Y. Zhang, Z. Bian, Y. Bu, X. Chen, T. Zhu, Z. Wang, J. Wang, S. Kawi, Q. Zhong, Efficient and stable nanoporous functional composited electrocatalyst derived from Zn/Co-bimetallic zeolitic imidazolate frameworks for oxygen reduction reaction in alkaline media, Electrochim. Acta 299 (2019) 610-617.

[32] C. Qian, X. Guo, W. Zhang, H. Yang, Y. Qian, F. Xu, S. Qian, S. Lin, T. Fan, Co3O4 nanoparticles on porous bio-carbon substrate as catalyst for oxygen reduction reaction, Micropor. Mesopor. Mat., 277 (2019) 45-51.

[33] G. Ye, Q. He, S. Liu, K. Zhao, Y. Su, W. Zhu, R. Huang, Z. He, Cage-confinement of gas-phase ferrocene in zeolitic imidazolate frameworks to synthesize high-loading and atomically dispersed Fe-N codoped carbon for efficient oxygen reduction reaction, J. Mater. Chem. A 7 (2019) 16508-16515.

[34] H. Wang, L.R. Grabstanowicz, H.M. Barkholtz, D. Rebollar, Z.B. Kaiser, D. Zhao, B.H. Chen, D.J. Liu, Impacts of imidazolate ligand on performance of zeolitic-imidazolate framework-derived oxygen reduction catalysts, ACS Energy Lett. 4 (2019) 2500-2507.

[35] G. Li, K. Zheng, C. Xu, An ingenious approach for ZIFs derived N-doped hierarchical porous carbon hybrids with FeCo alloy nanoparticles as

efficient bifunctional oxygen electrocatalysts, Appl. Surf. Sci. 487 (2019) 496-502.

[36] M. Thomas, R. Illathvalappil, S. Kurungot, B.N. Nair, A.P. Mohamed, G.M. Anilkumar, T. Yamaguchi, U.S. Hareesh, Morphological ensembles of N-doped porous carbon derived from ZIF-8/Fe-graphene nanocomposites: processing and electrocatalytic studies, Chem. Select 3 (2018) 8688-8697.

[37] Y. Ye, F. Cai, C. Yan, Y. Li, G. Wang, X. Bao, Two-step pyrolysis of ZIF-8 functionalized with ammonium ferric citrate for efficient oxygen reduction reaction, J. Energy Chem. 26 (2017) 1174-1180.

[38] Y. Ye, F. Cai, H. Li, H. Wu, G. Wang, Y. Li, S. Miao, S. Xie, R. Si, J. Wang, X. Bao, Surface functionalization of ZIF-8 with ammonium ferric citrate toward high exposure of Fe-N active sites for efficient oxygen and carbon dioxide electroreduction, Nano Energy 38 (2017) 281-289.

[39] J. Wang, G. Han, L. Wang, L. Du, G. Chen, Y. Gao, Y. Ma, C. Du, X. Cheng, P. Zuo, G. Yin, ZIF-8 with ferrocene encapsulated: a promising precursor to single-atom Fe embedded nitrogen-doped carbon as highly efficient catalyst for oxygen electroreduction, Small 14 (2018) 1704282.

[40] C. Zhang, Y.C. Wang, B. An, R. Huang, C. Wang, Z. Zhou, W. Lin, Networking pyrolyzed zeolitic imidazolate frameworks by carbon nanotubes improves conductivity and enhances oxygen-reduction

performance in polymer-electrolyte-membrane fuel cells, Adv. Mater. 29 (2017) 1604556.

[41] V. Armel, S. Hindocha, F. Salles, S. Bennett, D. Jones, F. Jaouen, Structural descriptors of zeolitic-lmidazolate frameworks are keys to the activity of Fe-N-C catalysts, J. Am. Chem. Soc. 139 (2017) 453-464.

[42] H.M. Barkholtz, L. Chong, Z.B. Kaiser, D.J. Liu, Non-precious metal catalysts prepared by zeolitic imidazolate frameworks: the ligand influence to morphology and performance, Fuel Cells 16 (2016) 428-433.

[43] D. Zhou, L. Yang, L. Yu, J. Kong, X. Yao, W. Liu, Z. Xu, X. Lu, Fe/N/C hollow nanospheres by Fe(iii)-dopamine complexation-assisted one-pot doping as nonprecious-metal electrocatalysts for oxygen reduction, Nanoscale 7 (2015) 1501-1509.

[44] Y. Li, T. Liu, W. Yang, Z. Zhu, Y. Zhai, W. Gu, C. Zhu, Multiscale porous Fe-N-C networks as highly efficient catalysts for the oxygen reduction reaction, Nanoscale 11 (2019) 19506-19511.

[45] J. Li, S. Chen, W. Li, R. Wu, S. Ibraheem, J. Li, W. Ding, L. Li, Z. Wei, A eutectic salt-assisted semi-closed pyrolysis route to fabricate high-density active-site hierarchically porous Fe/N/C catalysts for the oxygen reduction reaction, J. Mater. Chem. A 6 (2018) 15504-15509.

[46] J. Wang, Z. Huang, W. Liu, C. Chang, H. Tang, Z. Li, W. Chen, C. Jia, T. Yao, S. Wei, Y. Wu, Y. Li, Design of N-coordinated dual-metal sites: a

stable and active Pt-Free catalyst for acidic oxygen reduction reaction, J. Am. Chem. Soc. 139 (2017) 17281-17284.

[47] H. Zhang, S. Ding, S. Hwang, X. Zhao, D. Su, H. Xu, H. Yang, G. Wu, Atomically dispersed iron cathode catalysts derived from binary ligand-based zeolitic imidazolate frameworks with enhanced stability for PEM fuel cells, J. Electrochem. Soc. 166 (2019) F3116-F3122.

[48] J. Han, X. Meng, L. Lu, J. Bian, Z. Li, C. Sun, Single-atom Fe-Nx-C as an efficient electrocatalyst for Zinc–air batteries, Adv. Funct. Mater. 29 (2019) 1808872.

[49] W. Yang, X. Liu, X. Yue, J. Jia, S. Guo, Bamboo-like carbon nanotube/Fe3C nanoparticle hybrids and their highly efficient catalysis for oxygen reduction, J. Am. Chem. Soc. 137 (2015) 1436-1439.

[50] W.J. Jiang, L. Gu, L. Li, Y. Zhang, X. Zhang, L.J. Zhang, J.Q. Wang, J.S. Hu, Z. Wei, L.J. Wan, Understanding the high activity of Fe-N-C electrocatalysts in oxygen reduction: Fe/Fe3C nanoparticles boost the activity of Fe-N-x, J. Am. Chem. Soc. 138 (2016) 3570-3578.

[51] H. Wang, F.X. Yin, N. Liu, R.H. Kou, X.B. He, C.J. Sun, B.H. Chen, D.J. Liu, H.Q. Yin, Engineering Fe–Fe3C@Fe–N–C active sites and hybrid structures from dual metal–organic frameworks for oxygen reduction reaction in H2–O2 fuel cell and Li–O2 battery, Adv. Funct. Mater. 29 (2019) 1901531.

[52] H.J. Fan, M. Knez, R. Scholz, K. Nielsch, E. Pippel, D. Hesse, M. Zacharias, U. Gösele, Monocrystalline spinel nanotube fabrication based on the Kirkendall effect, Nat. Mater. 5 (2006) 627-631.

[53] F. Pan, J. Jin, X. Fu, Q. Liu, J. Zhang, Advanced oxygen reduction electrocatalyst based on nitrogen-doped graphene derived from edible sugar and urea, ACS Appl. Mater. Inter. 5 (2013) 11108-11114.

[54] X. Li, B.N. Popov, T. Kawahara, H. Yanagi, Non-precious metal catalysts synthesized from precursors of carbon, nitrogen, and transition metal for oxygen reduction in alkaline fuel cells, J. Power Sources 196 (2011) 1717-1722.

[55] Y. Zhao, K. Watanabe, K. Hashimoto, Self-supporting oxygen reduction electrocatalysts made from a nitrogen-rich network polymer, J. Am. Chem. Soc. 134 (2012) 19528-19531.

[56] H. Kim, K. Lee, S.I. Woo, Y. Jung, On the mechanism of enhanced oxygen reduction reaction in nitrogen-doped graphene nanoribbons, Phys. Chem. Chem. Phys. 13 (2011) 17505-17510.

[57] W. Ding, Z. Wei, S. Chen, X. Qi, T. Yang, J. Hu, D. Wang, L.J. Wan, S.F. Alvi, L. Li, Space-confinement-induced synthesis of pyridinic- and pyrrolic-nitrogen- doped graphene for the catalysis of oxygen reduction, Angew. Chem., Int. Ed. 52 (2013) 11755-11759.

[58] Z. Li, M. Shao, L. Zhou, R. Zhang, C. Zhang, M. Wei, D.G. Evans, X. Duan, Directed growth of metal-organic frameworks and their derived carbon-based network for efficient electrocatalytic oxygen reduction, Adv. Mater. 28 (2016) 2337-2344.

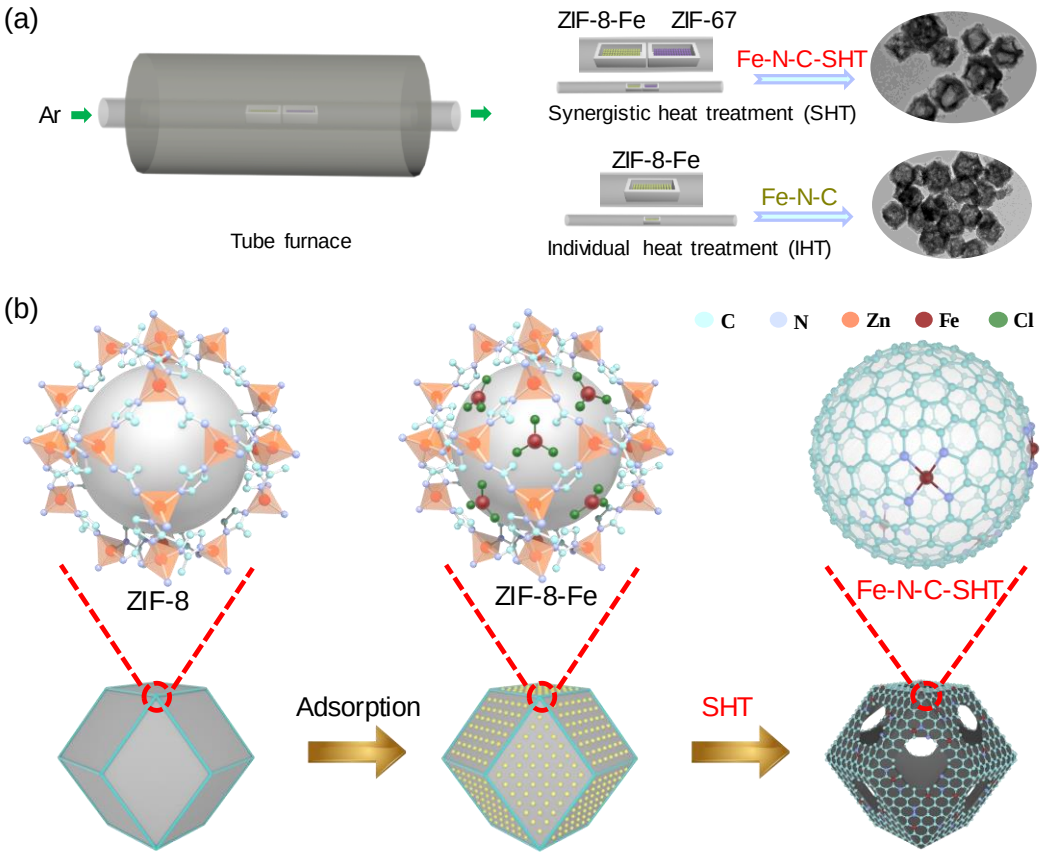

Fig. 1. (a) Schematic of individual heat treatment and synergistic heat treatment, (b) formation of synergistic heat treatment-derived hollow-mesoporous-microporous structure.

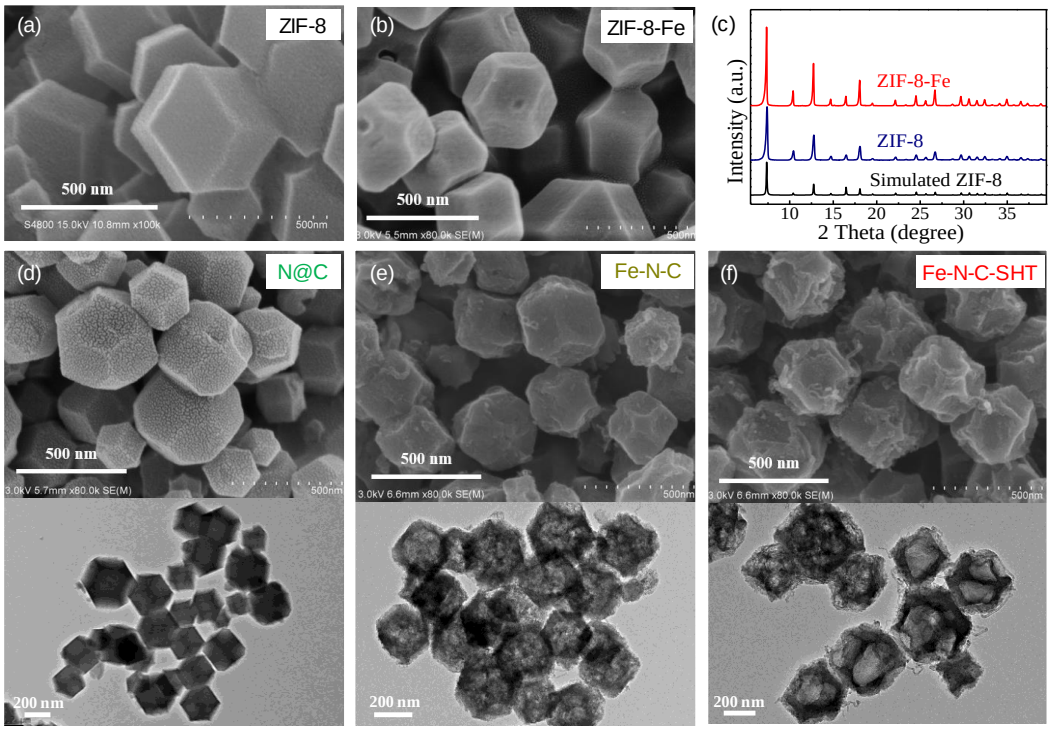

Fig. 2. Representative SEM images of (a) ZIF-8 and (b) ZIF-8-Fe. (c) XRD patterns of ZIF-8 (blue), ZIF-8-Fe (red), and simulated ZIF-8 (black). Representative SEM and TEM images of (d) N@C, (e) Fe-N-C, and (f) Fe-N-C-SHT.

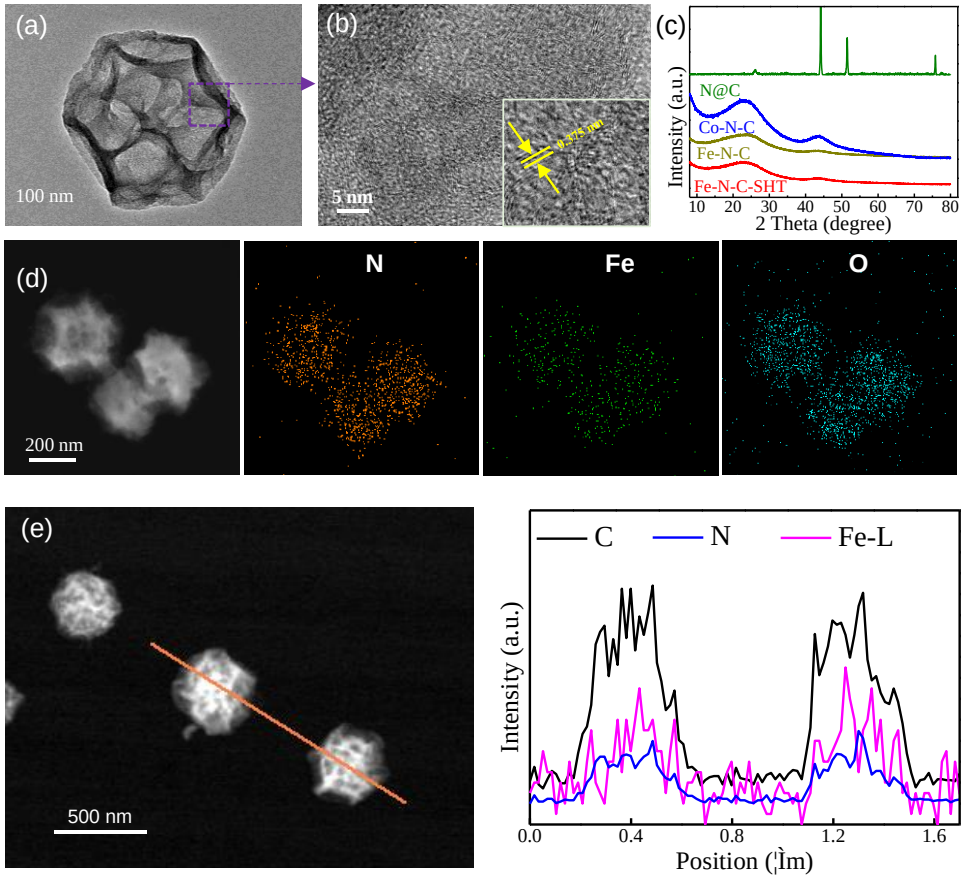

Fig. 3. (a, b) High-resolution TEM images of Fe-N-C-SHT. (c) XRD patterns of Fe-N-C-SHT (red), Fe-N-C (dark yellow), N@C (green), and Co-N-C (blue). (d) HAADF-STEM image and corresponding element mapping graphs of N (brown), Fe (dark green)

and O (dark blue), of Fe-N-C-SHT. (e) HAADF-STEM image and corresponding element line sweep curves of C (black), N (blue), and Fe (purple) of Fe-N-C-SHT.

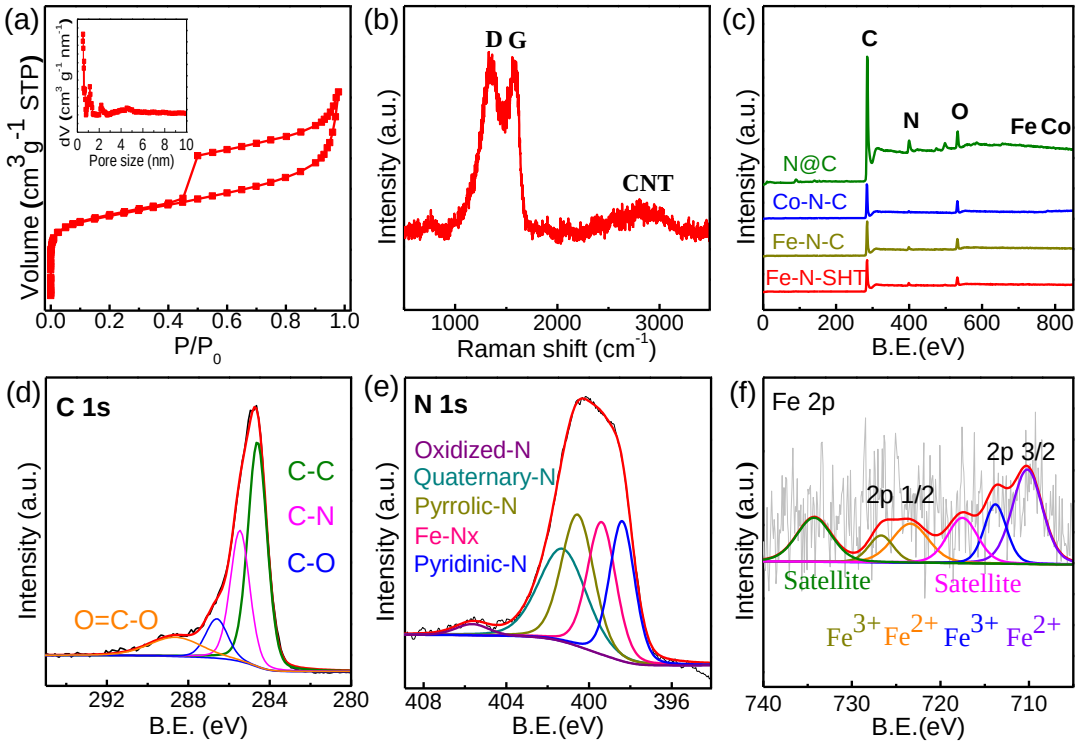

Fig. 4. (a) Nitrogen adsorption–desorption isotherm curve and pore size distribution (insert) of Fe-N-C-SHT. (b) Raman spectrum of Fe-N-C-SHT. (c) XPS spectra of Fe-N-C-SHT (red), Fe-N-C (dark yellow), N@C (green), and Co-N-C (blue). High-resolution XPS spectra of (d) C 1s, (e) N 1s, and (f) Fe 2p of Fe-N-C-SHT.

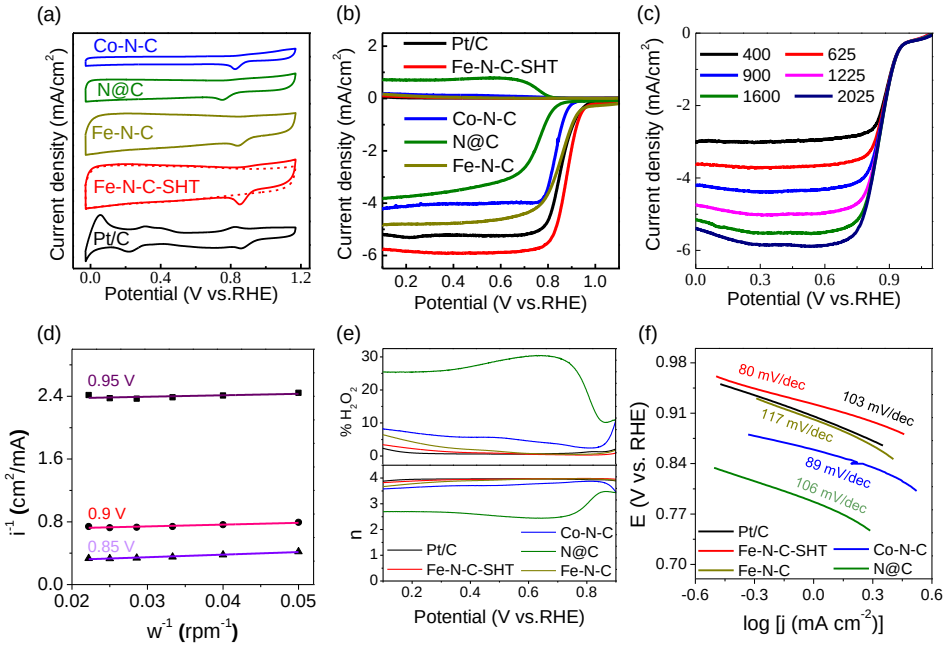

Fig. 5. (a) CV and (b) LSV curves of Pt/C (black), Fe-N-C-SHT (red), Fe-N-C (dark yellow), N@C (green), and Co-N-C (blue) in O_2-saturated 0.1 M KOH solution. The dotted line in (a) represents as CV curve in N_2-saturated 0.1 M KOH solution for Fe-N-C-SHT. (c) LSV curves of Fe-N-C-SHT recorded with different rotation rates from 400 to 2025 rpm. (d) K-L plots of Fe-N-C-SHT recorded at different potential values. (e) Electron transfer numbers and yield of H_2O_2 obtained with Fe-N-C-SHT catalysts and its reference samples. (f) Tafel plots of Fe-N-C-SHT at potential values of 0.95, 0.90 and 0.85 V.

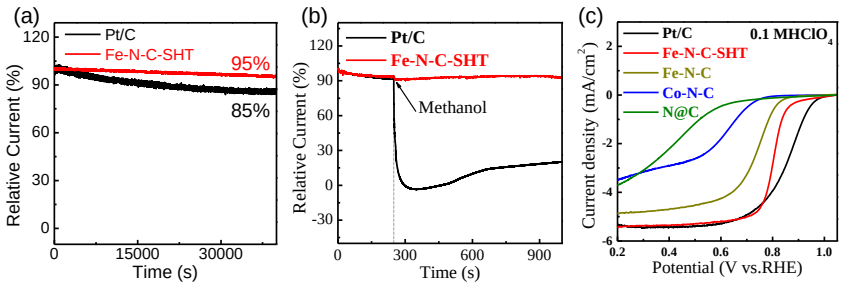

Fig. 6. (a) Current–time (i–t) chronoamperometric response of Fe-N-C-SHT at 0.7 V (vs. RHE) in 0.1 M KOH solution. (b) i–t chronoamperometric response of Fe-N-C-SHT and Pt/C catalysts at 0.7 V (vs. RHE) in O_2-saturated 0.1 M KOH solution with and without 3 M methanol added at 250 s; the rotation rate is 1600 rpm. (c) LSV curves of Fe-N-C-SHT and its reference samples in 0.1 M $HClO_4$ solution.

Graphitic abstract